

Unraveling volcano trend in OER of metal–organic frameworks with asymmetric configuration through energy band engineering

Jian Zhou^{a,1}, Zhichu Ren^{a,1}, Fei Qiao^a, Huiyu Gai^a, Shuai Qiu^a, Canhui Zhang^a, Xingkun Wang^b, Zongkun Chen^c, Heqing Jiang^b, Minghua Huang^{a,*}

^a School of Materials Science and Engineering, Ocean University of China, Qingdao 266100, China

^b Qingdao New Energy Shandong Laboratory, Qingdao Institute of Bioenergy and Bioprocess Technology Chinese Academy of Sciences, 189 Songling Road, Qingdao 266101, China

^c Physical Chemistry, University of Konstanz, Konstanz 78457, Germany



ARTICLE INFO

Keywords:

Metal-organic frameworks
Energy band engineering
Asymmetric electronic structure
D-band center
Oxygen evolution reaction

ABSTRACT

Local symmetry breaking of catalysts has emerged as an effective strategy for finely tuning oxygen evolution reaction (OER) activity, yet the fundamental comprehension regarding asymmetric structure-activity relationships remains limited. Here, we propose the energy band engineering to bridge the correlation between established asymmetric electronic structure and adsorption/desorption ability of reaction intermediates within metal-organic frameworks (MOFs). The deliberate synthesis of CoM-MOFs ($M=$ Cu, Ni, and Fe) with distinct coordination microenvironments enables the customization of asymmetric Co-O-M electronic structure. A volcano-shaped relationship can be revealed between calculated OER overpotential and average d-band center (E_d) energy level for both active Co sites and substituted M. The CoFe-MOF, located close to the summit, showcases the balanced reaction intermediate behavior and thus for enhanced OER activity. This work presents a promising approach to thoroughly understand asymmetric electronic structure-activity relationships from the perspective of energy band engineering and further guide the discovery of high-efficiency MOF-based OER catalysts.

1. Introduction

The oxygen evolution reaction (OER) holds paramount significance for the pursuit of numerous future applications in alternative energy conversion and storage technologies, including water electrolysis, fuel cells, and metal-air batteries [1–3]. Nevertheless, the sluggish reaction kinetics caused by the multi-step proton-coupled electron transfer leads to a relatively large overpotential involved in catalyzing OER, thereby imposing a significant constraint on its widespread implementation [4]. As well established, the OER activity is significantly correlated with adsorption behavior of oxygen-related intermediates (OH^* , O^* , and OOH^*) on active sites [5]. Fine catalytic activity control requires balancing the adsorption energy contributions [6]. Various strategies, including interface engineering [7], strain engineering [8], and defect engineering [9,10], have been consistently proposed for the design of earth-abundant and cost-effective OER catalysts. These methods aim to modify the coordination and electronic environments of OER catalysts, thereby adjusting the charger distribution and achieving optimized

adsorption of oxygen-related intermediates on the catalysts surface [11]. However, the complex correlation between the electronic structure and adsorption ability of reaction intermediates remains elusive, which restricts the comprehension of the underlying OER mechanisms and thus hampers the rational design of high-efficiency OER catalysts.

Recently, the precise engineering on asymmetric electronic distributions of the catalysts has been emerging as a promising strategy for fine-tuning OER performance [12–14]. The exclusive electronic structure acquired through local symmetry breaking, distinguishing from conventional symmetric structures, enables the achievement of efficient electron transfer and thus optimized energy levels for balanced oxygen-related intermediate adsorption [15]. For instance, Wu et al. constructed an asymmetric Ru-O-In electronic configuration that showcases an appropriate energy level with the reduced free energy barrier, resulting in impressive OER performance under acidic operating conditions [12]. Yao et al. constructed asymmetric backbone and side-chain conjugated polymer with different alkyl chain lengths, exhibiting the regulated charge distribution and thus improved catalytic activities

* Corresponding author.

E-mail address: huangminghua@ouc.edu.cn (M. Huang).

¹ These authors contributed equally to this work.

[13]. Our research group also proposed Co-N₃P₁ sites with asymmetric electronic structures, exhibiting the appropriate d-band center of active Co sites for optimized adsorption ability [14]. Unfortunately, such structure design primarily depends on an empirical trial-and-error method, while the precise and effective modulation of charger distribution around active sites has been far behind, let alone comprehensively elucidating the explicit asymmetric electronic structure-activity relationships.

Metal-organic frameworks (MOFs), featuring well-defined coordination environments, distinct active sites, and explicit electron transfer pathways, have been proposed as an ideal OER platform to explore the electronic structure-activity relationships [16,17]. Herein, energy band engineering is adopted to optimize a series of CoM-MOFs (M=Cu, Ni, and Fe), in which the charge distribution can be systematically customized by adjusting Co-O-M electronic structures through the disruption of the symmetrical coordination unit of active sites. The choice of Cu, Ni, and Fe is based on the following considerations. The π donation always occurs between Fe with unoccupied π -symmetry d-orbitals and the bridging ligand O²⁻, while the primary e⁻-e⁻ repulsion is recognized as the main interaction between Ni or Cu with fully filled π -symmetry d-orbitals and the bridging ligand O²⁻ [18]. It is worth noting that the degree of e⁻-e⁻ interaction is different for both Ni-O and Cu-O due to their distinct 3d electronic configurations. In these cases, the asymmetric electronic structures with diverse charger distribution around active sites could be established correspondingly. Five types of d-band center (E_d) energy level are therefore comprehensively and thoroughly investigated based on the modified coordination microenvironment within the MOF structure. Mechanistic insights reveal that the average E_d for both central Co sites and substituted M exhibits a volcano-shaped correlation with the calculated OER overpotential. The as-synthesized CoFe-MOF with asymmetric Co-O-Fe electronic structure is positioned near the summit of the volcano plot, featuring an appropriate E_d energy level, which results in balanced adsorption abilities of OH*/OOH* and thus for boosted OER activity. The advanced concept emphasized here is that the developed energy band engineering could be applied to in-depth understand the asymmetric electronic structure-activity and thus accelerate the discovery of highly active catalysts.

2. Experimental section

2.1. Materials

Nickel acetate tetrahydrate (Ni (CH₃COO)₂·4 H₂O; 99.9%), Iron acetate (Fe (CH₃COO)₂; 90.0%), Copper acetate monohydrate (Cu (CH₃COO)₂·H₂O; 99.0%), Cobalt (II) acetate tetrahydrate (Co (CH₃COO)₂·4 H₂O; 99.5%), 1,4-benzenedicarboxylic acid (H₂BDC; 99%), are all purchased from Aladdin Industrial Corporation. N, N-Dimethylformamide (DMF; AR), Acetonitrile (CH₃CN; AR), Potassium hydroxide (KOH; AR) is provided by Sinopharm Chemical Reagent Co., Ltd. 5%. Nafion solution and ruthenium oxide (RuO₂; 99.9%) are obtained from Sigma Aldrich Corporation. All reagents are analytically pure and used directly without any processing.

2.2. Synthesis of Co-MOF, CoCu-MOF, CoNi-MOF, and CoFe-MOF

A 20 mL glass bottle is employed for the synthesis of a series of MOF-based samples, taking the synthesis of Co-MOF as an illustrative example. Initially, a ligand solution consisting of 10 mg of H₂BDC dissolved in a mixture of 2 mL of DMF and 1 mL of CH₃CN is carefully introduced into the bottom of the glass bottle. Subsequently, a mixture of 1 mL of DMF and 1 mL of CH₃CN is added cautiously to prevent rapid mixing of the upper and lower solutions. Finally, 7.1 mg of Co (CH₃COO)₂·4 H₂O, dissolved in a mixture of 1 mL of DMF and 2 mL of CH₃CN, is also meticulously added to the bottle as the top layer. The glass bottle is then placed in the refrigerator for interfacial reaction at

low temperature, maintaining static conditions for 12 hours. This facilitates the controlled diffusion and enrichment of metal ions and ligands on the middle layer and the occurrence of the coordination reaction. Subsequently, the final precipitate is separated through centrifugation (10000 rpm, 20 min) using DMF and CHCl₃ three times, respectively. After naturally drying the resulting product in the fume hood, purple products are obtained for measurement.

A comparable method is employed for the synthesis of various Co-based MOFs, except for utilizing distinct metal precursors, namely Ni (CH₃COO)₂·4 H₂O, Cu (CH₃COO)₂·2 H₂O, and Fe (CH₃COO)₂ at the initial stage. The overall moles of metal ions are consistently maintained at 0.04 mmol. Based on the diverse transition metal heteroatoms, the resulting samples are denoted as CoCu-MOF, CoNi-MOF, and CoFe-MOF.

2.3. Electrochemical measurements

Electrochemical measurements are conducted using a conventional three-electrode system on a CH Instruments 760E electrochemical workstation at room temperature. A carbon cloth (CC) electrode, serves as the working electrode, while a graphite rod and Hg/HgO (1 M KOH, pH = 14) are utilized as the counter and reference electrodes in an alkaline aqueous solution.

The pretreatment of the CC involves sequential immersion in acetone (30 mL), deionized ethanol (30 mL), and deionized water (30 mL) in an ultrasonic machine for 20 minutes each, followed by drying in a vacuum oven at 50°C. The catalyst ink is prepared by dispersing 5 mg of the MOF powders in a water/isopropanol/naphthal (4:1:0.1 v/v/v) mixed solvent and then achieving a catalyst ink through ultrasonication. Subsequently, 50 μ L of the catalyst suspension is drop-cast onto the CC electrode surface and air-dried at room temperature before OER testing, with a mass loading of 1 mg cm⁻² for all samples.

All electrochemical tests are performed in 1 M KOH (pH=14) aqueous solution. Prior to OER activity testing, the catalyst undergoes electrochemical activation through linear sweep voltammetry (LSV) at a scan rate of 50 mV s⁻¹ until the curves stabilize. LSV curves are then collected at a scan rate of 5 mV s⁻¹. All potentials used in this study are converted into RHE using the following equation: E (RHE) = E (Hg/HgO) + 0.0591 pH + 0.098. The Tafel slope is fitted by the Tafel equation [η = b log(j) + a].

Electrochemical impedance spectroscopy (EIS) is conducted from 10⁵ to 0.01 Hz with the potential set sufficiently high to ensure OER occurrence. The double-layer capacitance (C_{dl}) is measured in a non-Faradaic region (0.4–0.5 V versus Hg/HgO) at various scan rates (v = 20, 40, 60, 80, 100, and 120 mV·s⁻¹). The electrochemical active surface area (ECSA) of the catalyst is calculated from the C_{dl} values according to the equation ECSA = C_{dl}/C_s . The specific capacitance (C_s) represents the capacitance of an atomically smooth planar surface per unit area under identical electrolyte conditions, typically ranging from 0.02 to 0.06 mF cm⁻². Based on our catalytic surface, C_s is typically estimated to be 0.04 mF cm⁻². Long-term stability tests are assessed via chronopotentiometry measurements at a current density of 10 mA·cm⁻² without iR compensation. All polarization curves are corrected using IR drop compensation.

2.4. Materials characterization

The morphology and structure of the synthesized MOFs are characterized by transmission electron microscopy (TEM), high-resolution transmission electron microscopy (HRTEM), energy-dispersive X-ray spectroscopy (EDS analytical data). X-ray diffraction (XRD) patterns are recorded by a Bruker D8 Advance diffractometer operated at 40 kV and 40 mA with a Cu K α radiation (λ = 1.54178 Å). Fourier transform infrared (FT-IR) spectra measurement is performed in the range of 400–4000 cm⁻¹ with the sample pelleted using KBr powders on Nexus at room temperature. Raman spectroscopy is performed with a Thermo Fisher spectrometer equipped with helium-neon (633 nm) and argon

(532 nm) lasers. The X-ray photoelectron spectra (XPS) are recorded on the Thermal Scientific ESCALAB 250Xi spectrometer. The X-ray absorption spectroscopy (XAS) measurements of Co and Fe K-edge are performed at the beamline BL14W1 in Shanghai Synchrotron Radiation Facility.

3. Results and discussion

3.1. Theoretical analysis

The conventional OER process with complex four-electron transfer steps involves the adsorption of OH*, O*, and OOH*, as well as the subsequent desorption of O₂ on the catalyst surface. Since the energy of 4.92 eV is required to trigger the water oxidation process at the standard conditions, the reaction barrier energy for each step should ideally be 1.23 eV [19]. Actually, the thermodynamic inhibition of at least one step usually exceeds 1.23 eV, thereby resulting in a higher calculated overpotential (η) for OER [20]. To effectively reduce η for the enhanced OER activity, the adsorption/desorption abilities of oxygen-related intermediates should be finely optimized on the catalyst surface [21–23]. In terms of the symmetric Co-O-Co structure of Co-MOF, electron transfer is constrained due to both sides of the bridging oxygen being the same metal, hindering the enhancement of transformation efficiency for oxygen intermediates. However, the asymmetric Co-O-M structure within CoM-MOFs allows for controlled electron transfer between Co and M atoms through the O 2p orbitals (Fig. 1a). The gradient orbital coupling of Co-O-M enables more flexible electronic interactions between 3d orbitals of Co/M and the O 2p orbitals of reaction intermediates (OH*, O*, and OOH*), contributing to the boosted OER activity. Such interaction can lead to the formation of bonding and antibonding states. The electron filling of the bonding states is typically full as they are distant from the Fermi level (E_F), while that of

antibonding states is associated with these energy states relative to E_F and contributes to the bond strength (Fig. 1b). Given that the energy of antibonding states is generally higher than that of d states, the energy level of E_d holds the potential to characterize the interaction between active sites and reaction intermediates [27]. Therefore, the energy band engineering derived from the gradient orbital coupling in the Co–O–M unit can theoretically bridge the significant gap between the asymmetric electronic structure and the adsorption/desorption abilities of oxygen-related intermediates.

3.2. Materials synthesis and characterization

As schematically shown in Fig. S1, the synthesis of CoM-MOF catalysts is carried out using an interface-mediated method [28]. This method involves the utilization of three-layer solvents consisting of an upper layer (DMF: CH₃CN=2:1), an intermediate layer (DMF: CH₃CN=1:1), and a bottom layer (DMF: CH₃CN=1:2), which are miscible but have different densities. Mixed Co–M (M= Cu, Ni, and Fe) metal ions and the terephthalic acid (H₂BDC) ligand are introduced to the upper layer and bottom layer, respectively. They will meet at the intermediate layer to drive the coordination reaction for generating a series of bimetallic CoM-MOFs (CoFe-MOF, CoCu-MOF, CoNi-MOF). The monometallic Co-MOF is also synthesized for comparison through a similar strategy.

The X-ray diffraction (XRD) patterns presented in Fig. 2a are utilized to analyze the crystal structures of CoM-MOFs. The diffraction peaks can be captured at about 8.8, 15.6, and 17.6° corresponding to the (200), (001), and (202) phases, which is consistent well with that of the simulated Co₂(OH)₂(C₈H₄O₄) MOF structure (Fig. S2) [27,29]. Fourier transforms infrared (FT-IR) spectra are employed to investigate the functional groups in the range of 4000–400 cm⁻¹ (Fig. 2b). The absorption peaks centered at ca. 539 cm⁻¹ can be assigned to the

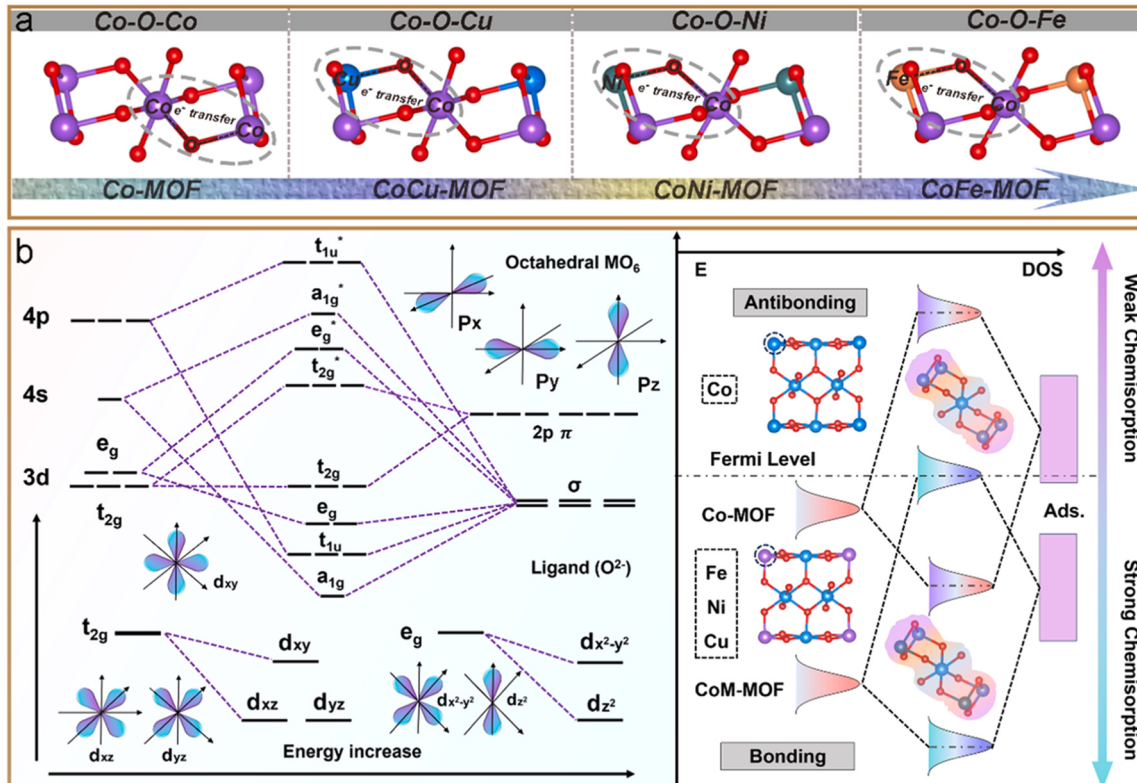


Fig. 1. a) The detailed coordination environment of Co-MOF, CoCu-MOF, CoNi-MOF, CoFe-MOF. b) Schematic illustration of bond formation between the catalyst surface and the oxygen-related intermediates (Ads.). The orbital coupling of valence 3d, 4 s, and 4p orbitals with mixing orbitals of bridged O atoms is shown for the basic MO₆ unit.

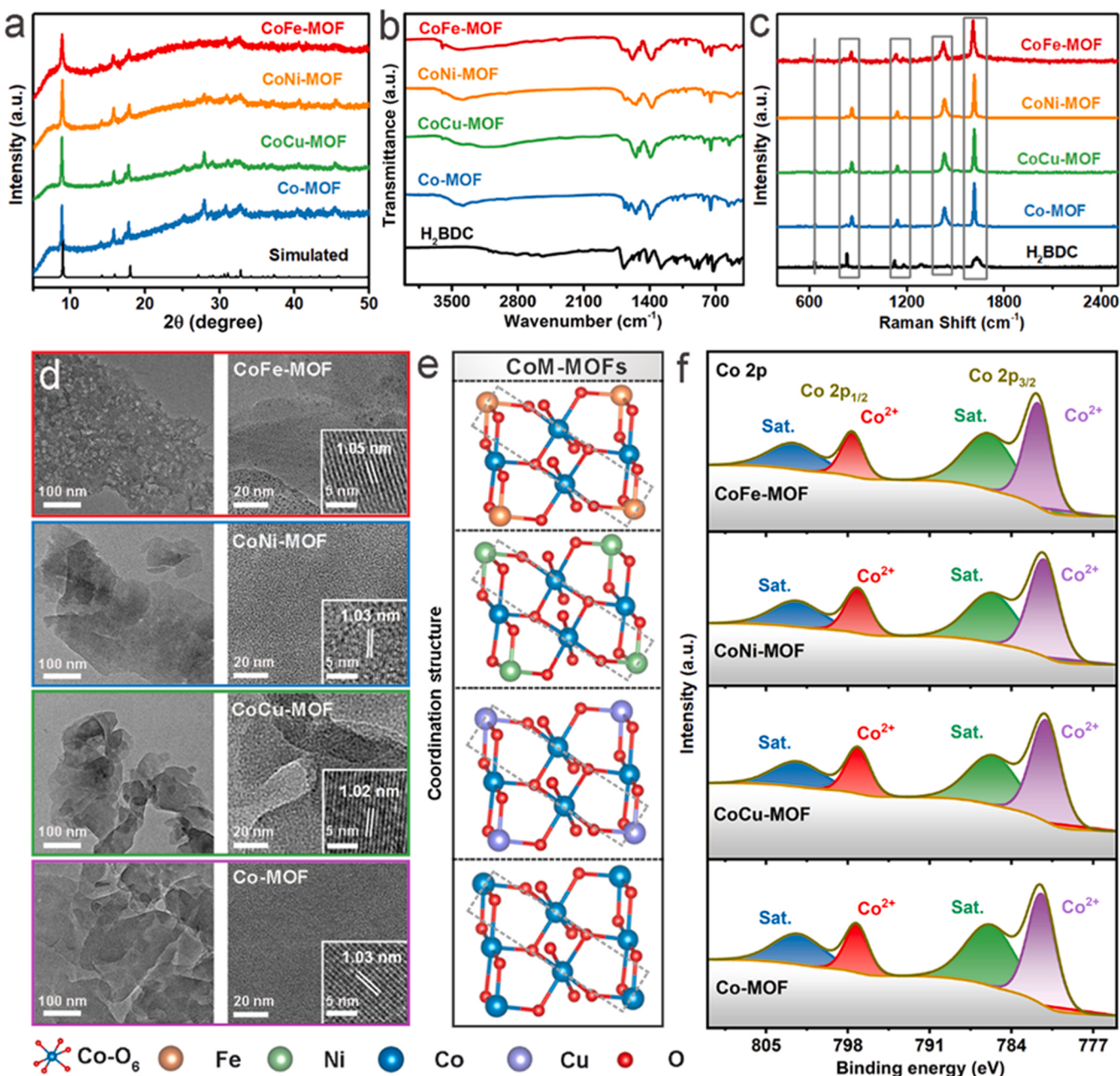


Fig. 2. a) XRD patterns, b) FT-IR and c) Raman spectra for Co-MOF and Co-M-MOFs (M=Co, Ni, and Fe). d) TEM images and corresponding HRTEM images of the as-synthesized Co-MOF, CoCu-MOF, and CoNi-MOF, as well as CoFe-MOF. e) Coordination structure and f) Co 2p XPS spectra of Co-MOF and Co-M-MOFs (M=Co, Ni, and Fe).

coordination vibration between the metal site and carboxylic groups of organic H₂BDC linker, confirming the successful formation of metal-oxygen bonds within the synthesized MOF structure [30,31]. The existence of absorption peaks at ca. 750 cm⁻¹ and 3420 cm⁻¹ are attributed to the C-H and O-H stretching vibration within the benzene ring, respectively. The captured peaks at ca. 1386 cm⁻¹ and 1575 cm⁻¹ are associated with the symmetric and asymmetric coordination stretching vibrations between the metal center and the carboxylic group of the organic ligand [32,33]. The presence of such hydrophilic carboxylic groups on the surface of MOF structure may be favorable to promoting water adsorption in catalyzing OER. The peaks at ca. 632 cm⁻¹ and 860 cm⁻¹ observed from Raman spectra can be ascribed to C-H stretching regions of the benzene ring, while the peak at 1136 cm⁻¹ is attributed to the H₂BDC coordinated vibration (Fig. 2c).

The bonds around 1341 cm⁻¹ and 1609 cm⁻¹ indicate the presence of coordinated -COO⁻ groups, reflecting the symmetric and asymmetric vibrations of stretching modes, respectively [32].

Transmission electron microscopy (TEM) is first used to investigate the detailed morphology and structure of CoM-MOFs, as shown in Fig. S3. As observed, the as-synthesized Co-MOF exhibits the typical 2D ultrathin nanosheets structures. Upon the incorporation of M into Co-MOF, the 2D nanosheet structure can be retained for CoFe-MOF, CoNi-MOF, and CoCu-MOF. It is worth noting that the hierarchical pores observed on the surface of the CoFe-MOF are not only conducive to exposing numerous active sites in MOF structure but also beneficial to improving mass transport of the oxygen-related intermediates, thereby enhancing the catalytic OER performance [34–36]. The high-resolution transmission electron microscopy (HRTEM) images reveal that the

lattice fringes spacings of Co-MOF, CoCu-MOF, CoNi-MOF, and CoFe-MOF are 1.03, 1.02, 1.03, and 1.05 nm, respectively, which can be indexed to the corresponding (200) crystal plane of these MOFs (Fig. 2d). The corresponding elemental mapping image showcases the uniform distribution of the C, O, Co, and Fe/Ni/Cu within the CoM-MOFs, as depicted in energy dispersion spectrum (EDS) results (Fig. S4,5).

X-ray photoelectron spectroscopy (XPS) is conducted to investigate the surface chemical composition and electronic state of bimetallic CoM-MOF samples. The pure H₂BDC and monometallic Co-MOF are also performed for comparison. Fig. 2e exhibits the coordination environment within the MOF structure in detail. As shown in Fig. S6, the presence of C, O, Co, and incorporated Fe, Cu, and Ni are confirmed by the XPS survey spectra, consistent well with the EDS mapping results. In comparison with pure H₂BDC, the high-resolution C 1 s and O 1 s spectra reveal the presence of newly formed C-O and Co (Fe/Ni/Cu)-O bonds [37], indicating the successful coordination between metal ions and the H₂BDC ligand (Fig. S7,8). For the high-resolution Fe 2p XPS spectra in CoFe-MOF, the Fe 2p_{3/2} (713.1 eV) and Fe 2p_{1/2} (723.6 eV) peaks,[24] as well as associated satellite peaks could be significantly observed, indicating the existence of Fe³⁺ oxidation state (Fig. S9). Similarly, the high-resolution Ni and Cu 2p XPS spectra demonstrate the existence of Ni²⁺ and Cu²⁺ in CoNi-MOF and CoCu-MOF [38,39], respectively (Fig. S10). The Co 2p spectrum of CoFe-MOF (Fig. 2f) can be

deconvoluted into four individual peaks assigned to Co²⁺ and the corresponding satellites, respectively. The negative shift in Co 2p_{3/2} binding energies observed for both CoCu-MOF (781.1 eV) and CoNi-MOF (781.2 eV) compared to Co-MOF (781.4 eV) indicates the accumulation of electrons around Co sites in these bimetallic MOFs. The binding energies in Co 2p_{3/2} of the CoFe-MOF (781.7 eV) shift to a higher level for 0.3 eV in contrast to Co-MOF (781.4 eV), indicating the electron transfer from Co atoms to Fe atoms. Such phenomenon suggests the localized electrons can be correspondingly redistributed by constructing the asymmetric Co-O-M electronic structures.

To further understand the local electronic configuration and atomic structures of Co-MOF and CoFe-MOF, X-ray absorption spectroscopy (XAS) is also performed. The Co K-edge X-ray absorption near-edge structure (XANES) spectra reveal that both Co-MOF and CoFe-MOF possess a similar signal close to that of CoO [40,41], signifying the comparable cation coordination environment (Fig. 3a). Through the detailed analysis of the first derivative of the XANES data, the corresponding valence state of the Co atoms is estimated by determining the E₀ values (the first inflection point on the absorption edge), as shown in Fig. 3b. It can be observed that the average valence state of Co atoms in CoFe-MOF is +2.4, which is higher than that of Co-MOF (+2.1), indicating the redistribution of the local electrons through the established asymmetric Co-O-Fe electronic structure. It has been reported that unfilled metal 3d e_g states, i.e., dx² and dz², play a pivotal role in the

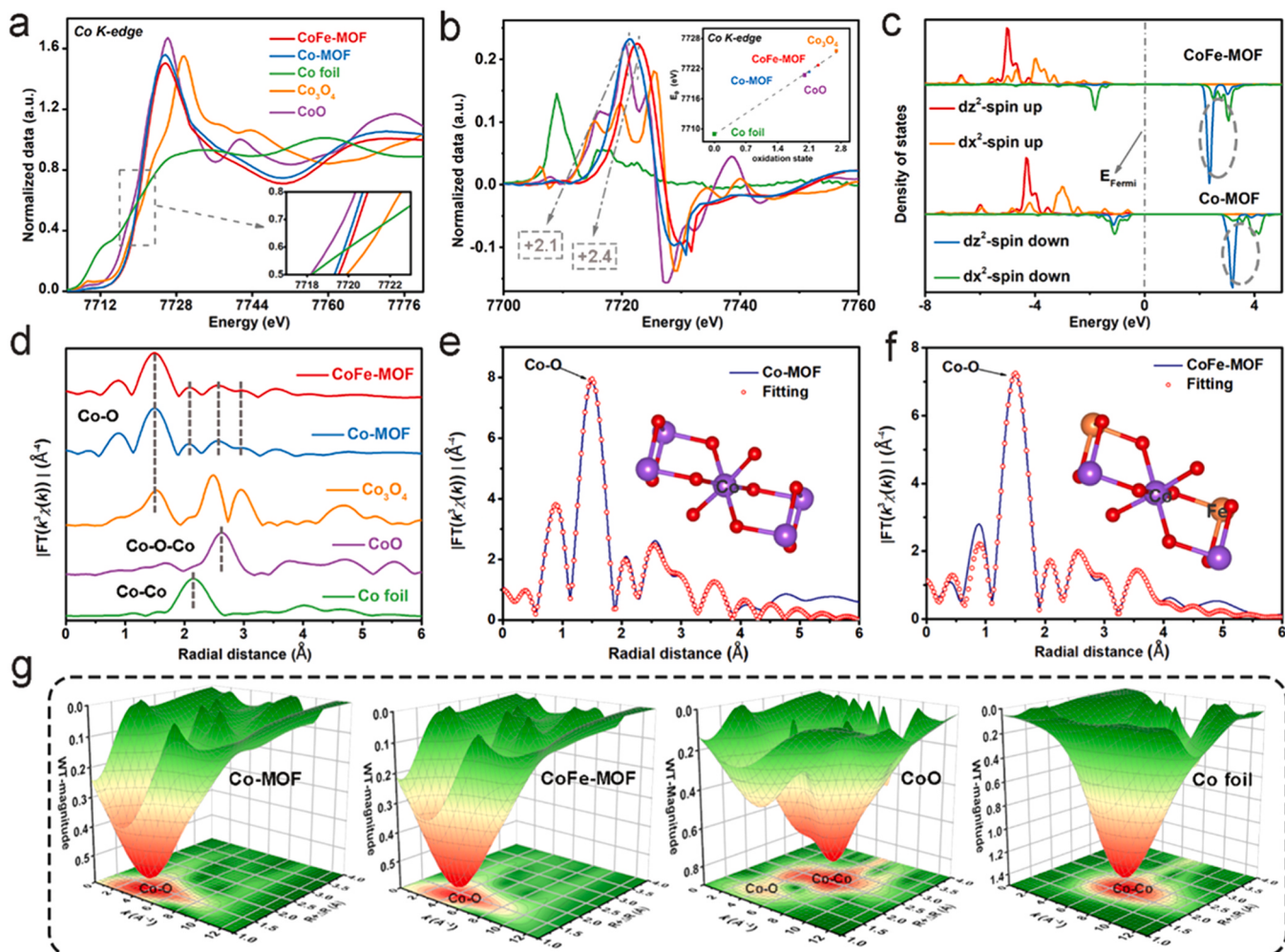


Fig. 3. a) Normalized Co K-edge XANES spectra of Co-MOF, CoFe-MOF, and the related references. b) Correlation between Co K-edge threshold value (E_0) and oxidation state for Co-MOF, CoFe-MOF and two reference materials. c) Projected 3d e_g density of states of Co site in Co-MOF, and CoFe-MOF, dz², and dx² represent different orientations of 3d e_g orbitals. Fermi level is set to zero. d) FT profiles of Co K-edge k³-weighted EXAFS data for Co-MOF, CoFe-MOF, and the related references. The k³-weighted EXAFS fitting curves at R space for the e) Co-MOF and f) CoFe-MOF. g) WT-EXAFS of Co-MOF, CoFe-MOF, CoO and Co foil.

pursuit of optimized electronic interactions [42,43]. Therefore, detailed calculations of the corresponding projected density of states (PDOS) on the e_g orbital are also performed in Fig. 3c. Compared with that of Co-MOF, the density of the unoccupied e_g state decreases for CoFe-MOF after the Fe-incorporation. The number of e_g electrons is found to be approximately 2.3 in the Co atom within CoFe-MOF, which is lower than the value of 2.5 observed for the Co atom in Co-MOF (Fig. S11). These results indicate the electronic structure of active Co sites could be well tailored following the formation of an asymmetric Co-O-Fe unit, in which the valence state of Co can be increased through the charge transfer from Co^{2+} to Fe^{3+} via the bridging O^2- . Such change could be advantageous for optimizing the adsorption/desorption of oxygen-related species (OH^* , OOH^* , and O^*) and, consequently, enhancing the OER activity [44].

The Fourier transform (FT) k^3 -weighted extended X-ray absorption fine structure (FT-EXAFS) spectra are shown in Fig. 3d. For both Co-MOF and CoFe-MOF, a prominent peak located at about 1.5 \AA could be attributed to Co-O bond at the first shell, with no detection of the Co-Co peaks. The other relatively weak peaks are associated with Co-C (2.36 \AA), Co-O (2.86 \AA), and Co-O-Co (3.25 \AA) bonds in the higher shells, respectively [16]. Moreover, the coordination configuration of

Co-MOF and CoFe-MOF is further confirmed by theoretical calculations (Table S1 and Fig. S12-14). The coordination number of Co-O is calculated as 5.9 in the first coordination shell of Co-MOF. This number decreases to 5.6 for CoFe-MOF, highlighting the presence of coordinatively unsaturated sites within the CoFe-MOF (Fig. 3e, f). The wavelet transforms (WT) analysis for the k^3 -weighted Co K-edge EXAFS curves manifest the prominent signal at ca. 3.8 \AA^{-1} attributed to the Co-O bond for both Co-MOF and CoFe-MOF (Fig. 3g). The signal associated with Co-Co bonds has been captured in the Co foil but not in Co-MOF and CoFe-MOF, implying the presence of atomically dispersed Co sites within the MOF structure [45].

Inspired by the optimized chemical component and the flexible asymmetric electronic structure, we first perform the OER measurements for the CoM-MOFs catalysts in an alkaline medium. As shown in Fig. 4a, the OER activities for CoM-MOFs and commercial RuO₂ are appraised by linear sweep voltammetry (LSV) curves. The CoFe-MOF exhibits the lowest overpotential of 236 mV at the current density of 10 mA cm^{-2} , which is significantly superior to those of CoNi-MOF (299 mV), CoCu-MOF (318 mV), Co-MOF (363 mV) and commercial RuO₂ catalyst (360 mV). It's worth noting that the same activity trend of CoM-MOFs is also observed at high current densities of 50 and

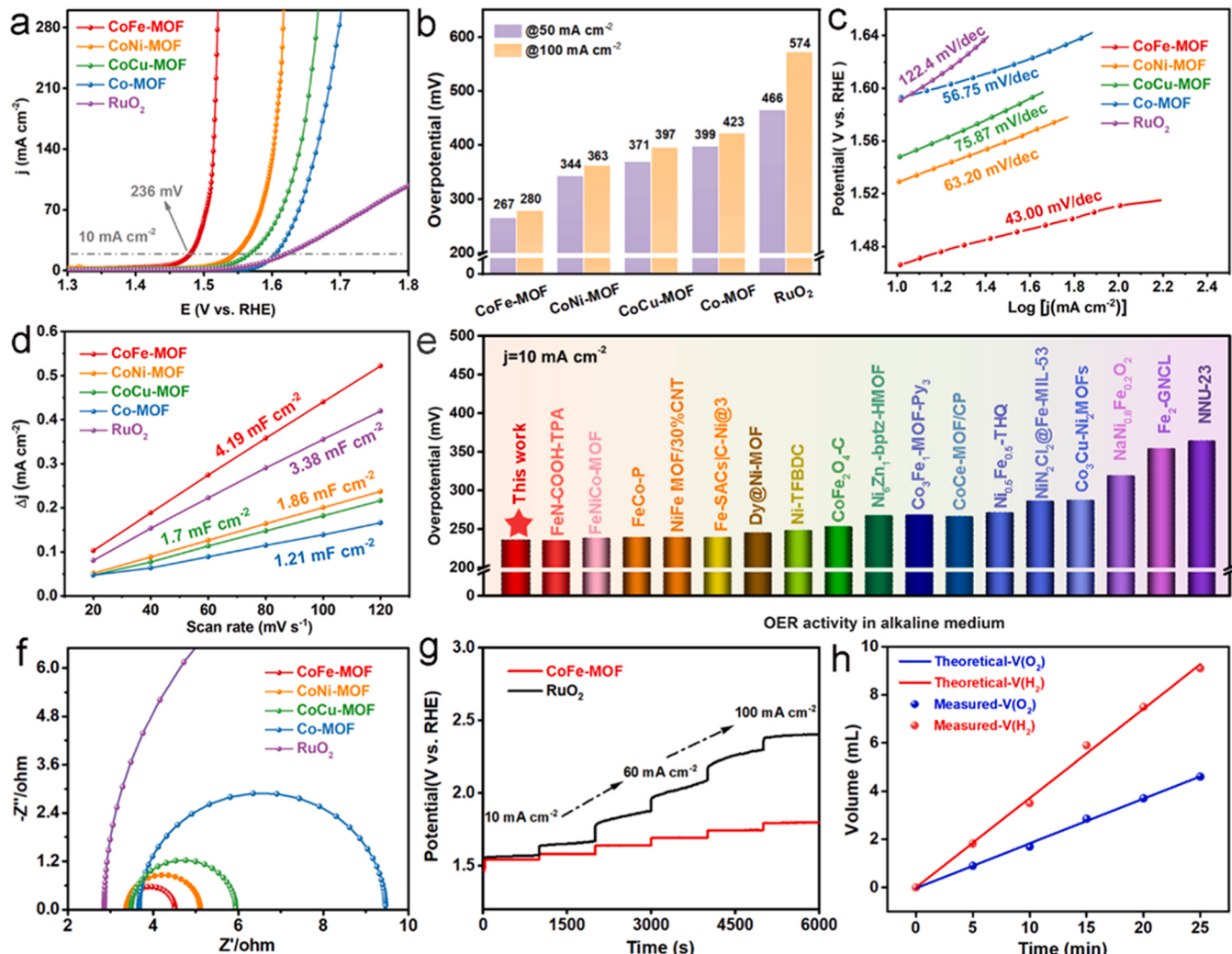


Fig. 4. a) LSV curves of Co-MOF, CoM-MOFs (M=Cu, Ni, and Fe) and RuO₂ in 1 m KOH, b) overpotential of Co-MOF and CoM-MOFs required for $j = 50$, and 100 mA cm^{-2} . c) the calculated Tafel plots, and d) the obtained C_{dl} . e) Comparison of the OER overpotential to drive the current density of 10 mA cm^{-2} for the CoFe-MOF with other recently reported non-noble metal OER catalysts. f) The corresponding Nyquist plots. g) Multi-current process obtained with the CoFe-MOF and commercial RuO₂ catalyst in 1 m KOH (the current density started at 10 mA cm^{-2} and stopped at 100 mA cm^{-2}). h) Comparison of the generated amounts of H_2 and O_2 between experimental and theoretical results for CoFe-MOF || Pt/C electrode during water splitting.

100 mA cm⁻² (Fig. 4b). To shed more insight into the catalytic reaction kinetics, the corresponding Tafel slope is also calculated (Fig. 4c). The CoFe-MOF shows the smallest Tafel value of 43 mV dec⁻¹, which is lower than CoNi-MOF (63.20 mV dec⁻¹), CoCu-MOF (75.87 mV dec⁻¹), Co-MOF (56.75 mV dec⁻¹), and commercial RuO₂ catalyst (122.40 mV dec⁻¹), showcasing its enhanced charge transfer and boosted reaction kinetics [46]. The electrochemically active surface area (ECSA), a key index relevant to the OER activity, is assessed from the double-layer capacitances (C_{dl}) via measuring cyclic voltammograms (CV) curves (Fig. S15). As shown in Fig. 4d, the C_{dl} value of CoFe-MOF (4.19 mF cm⁻²) is larger than those of CoNi-MOF (1.86 mF cm⁻²), CoCu-MOF (1.70 mF cm⁻²), Co-MOF (1.21 mF cm⁻²), and RuO₂ (3.38 mF cm⁻²). This result suggests that more accessible active sites are exposed on the surface after the Fe incorporation into Co-MOF. LSV curves are then normalized by ECSA to investigate the intrinsic activity of catalysts [31]. It is evident that the as-synthesized CoFe-MOF retains the smallest overpotential (300 mV at 3.75 mA cm⁻²) among all examined samples, indicating its superior intrinsic performance (Fig. S16). Based on the results mentioned above, the CoFe-MOF displays outstanding catalytic activity and long-time stability, which is even better than most of the MOF-based OER catalysts reported recently (Fig. 4e and Table S2). Electrochemical impedance spectroscopy (EIS) is then performed to further investigate the charge transfer resistance [47–49]. The Nyquist plots of CoM-MOFs are then fitted with the equivalent resistance-capacitance circuit, as depicted in Fig. S17 and Table S3. As observed in Fig. 4f, CoFe-MOF possesses the minimum semicircle diameter, exhibiting the lowest charge transfer resistance (R_{ct}) and the fastest charge transfer rate at the electrode-electrolyte interface. The turnover frequency (TOF) and mass activity (MA), regarded as the curial quantitative parameters to appraise the intrinsic OER activity, are also calculated (Fig. S18). Assuming all metal ions participate in the OER process, the higher value of TOF and MA (4.14 s⁻¹, 19.0 A g⁻¹) is obtained for the CoFe-MOF, prominently exceeding those of CoNi MOF (0.79 s⁻¹, 2.89 A g⁻¹), CoCu-MOF (0.22 s⁻¹, 1.95 A g⁻¹), Co-MOF (0.15 s⁻¹, 0.73 A g⁻¹) and commercial RuO₂ catalyst (0.20 s⁻¹, 1.37 A g⁻¹), verifying its enlarged accessible surface area and enhanced intrinsic activity.

Another essential criterion, i.e., long-term stability, is used to gain information on assessing the OER performance of the CoFe-MOF, in which chronopotentiometric curves at 10 mA cm⁻² are recorded (Fig. S19). Compared with commercial RuO₂, no significant increase in potential can be observed for CoFe-MOF, implying its extraordinary long-term durability. The CoFe-MOF also demonstrates superior long-term stability at high current densities, as evidenced by chronopotentiometric curves recorded at 50 and 100 mA cm⁻² (Fig. S20). The multi-step chronopotentiometric test is then performed over a wide current density range from 10 to 100 mA cm⁻². Note that the operating potential reaches a fixed value and maintains stable at each step, further proving the excellent stability of CoFe-MOF (Fig. 4g). The cycling stability is also conducted by successive CV scanning. Compared with the initial one, only a slight positive shift can be observed from the LSV curves after 1000 CV cycles, indicating the superior long-term cycling durability of CoFe-MOF (Fig. S21). It is noteworthy that the moderate coordination bonds between metal sites and the organic H₂BDC ligand can undergo decomposition upon attack by OH⁻ in alkaline solution [50–53]. After OER, the degraded ligand in CoM-MOFs is subsequently detected using UV-vis spectroscopy, as depicted in Fig. S22. As observed, the synthesized Co-MOF and CoM-MOFs (M = Fe, Ni, Cu) would go through similar decomposition processes in alkaline media and the presence of residual coordination ligands within the frameworks will decrease as metal cations transform into (oxy)hydroxides [31]. The maximal COO⁻ concentration is subsequently observed in CoFe-MOF, suggesting its pronounced inclination toward (oxy)hydroxide transformation [1]. Furthermore, TEM and XPS analysis is conducted to investigate the structural stability of CoFe-MOF post-OER (Figure S23). Remarkably, no significant changes in the morphology of CoFe-MOF are

observed after the OER test. In the Co 2p high-resolution XPS spectra, the presence of Co³⁺ is determined by peaks at 780.3 and 795.5 eV, indicating partial oxidation of Co²⁺ to Co³⁺ following the durability test [54–57]. However, due to the overlap of the Fe 2p_{3/2} signal with F 1 s in the XPS spectra, further analysis is not presented [31]. A two-electrode system is then assembled to evaluate overall water splitting by using the CoFe-MOF as anode and commercial Pt/C as the cathode (CoFe-MOF || Pt/C). As observed in Fig. S24, the CoFe-MOF || Pt/C possesses the smallest cell voltage of 1.52 V at 10 mA cm⁻², whereas 1.57 V is required for commercial RuO₂||Pt/C. Chronopotentiometry tests of assembled CoFe-MOF || Pt/C electrode reveal exceptional long-term durability, with only 2.5% increase of potential observed following continuous electrolysis over a period of 24 hours (Fig. S25). Additionally, the Faradaic efficiencies are measured at the current density of 10 mA cm⁻² using a Hoffman apparatus setup. As shown in Fig. 4h the hydrogen/oxygen yield rates match well with the theoretical value (2:1), which implies the high selectivity of H₂ and O₂ during the water splitting.

To further probe the catalytic mechanism of activity trend, a series of DFT+U calculations are conducted on the constructed CoM-MOFs model structures (Fig. S26). Fig. 5a shows the energy profiles for multi-step proton-coupled electron transfer during the OER process. The OH⁻ ion is absorbed on catalytic sites initially, followed by its reaction with another OH⁻ ion to produce absorbed atomic O and release electrons, along with H₂O. Subsequently, absorbed OOH forms as the absorbed atomic O reacts with an additional OH⁻ in the alkaline solution, ultimately leading to the generation of O₂ on active sites by reacting with further OH⁻ ions [33]. Given the crucial role of the appropriate interaction strength between the active metal sites and reaction intermediates in promising OER activity [58,59], we first calculate the Gibbs free energies of oxygen-related intermediates for Co-MOF and CoM-MOFs. For Co-MOF at U = 0 V, the largest reaction energy barriers (2.22 eV) are observed during the transformation from O^{*} to OOH^{*} (step iii), which is determined as the rate-determining step (RDS), as shown in Fig. 5b. Considering the presence of two different metal sites in CoM-MOFs, the reaction barrier for Co site and Cu site in CoCu-MOF, Co site and Ni site in CoNi-MOF, as well as Co site and Fe site in CoFe-MOF are calculated at U=0 V (Fig. 5c-h). It is evident that the reaction barriers for all examined Co sites are significantly lower than those for the corresponding M sites in CoM-MOFs (M = Cu, Ni, and Fe), respectively, suggesting the Co sites would serve as the active centers in catalyzing OER (Fig. S27). As observed, the RDS for CoFe-MOF is the adsorption of OH^{*} (step i), while those for CoCu-MOF and CoNi-MOF involve the transformation of O^{*} to OOH^{*} (step iii). These results indicate that the RDS could be correspondingly modified through the construction of an asymmetric Co-O-M structure. The theoretical overpotential (η) at U=1.23 eV for specific step is also calculated. As observed, the lowest calculated η is obtained for the CoFe-MOF with the smallest reaction barrier, exhibiting the best catalytic activity among all the investigated MOF structures (Fig. 5i). The η values follow a decreasing sequence: CoFe-MOF < CoNi-MOF < CoCu-MOF < Co-MOF, aligning with the aforementioned experimental observations of OER activity.

To deeply understand the correlation between asymmetric electronic structure and OER activity, state-of-the-art DFT simulations, encompassing the band structure, PDOS, and the energy level of the d-band center (E_d), are performed for Co-MOF and CoM-MOFs. We first construct and optimize a symmetric Co-O-Co electronic structure in Co-MOF, as well as asymmetric electronic structures of CoM-MOFs (Co-O-Cu, Co-O-Ni, and Co-O-Fe). The calculated energy band structure close to the Fermi level (E_F) of Co-MOF primarily comprises Co-3d states (Fig. 6a), whereas those of CoM-MOFs are composed of both Co-3d and M-3d states (Fig. 6b-d). Therefore, the E_d energy level can be applied to characterize the interaction between the oxygen-related intermediates and catalysts surface according to the d-band center theory [60–63]. The energy level of five E_d types, stemming from the various coordination microenvironments within the MOF structure [41,42], are deliberately

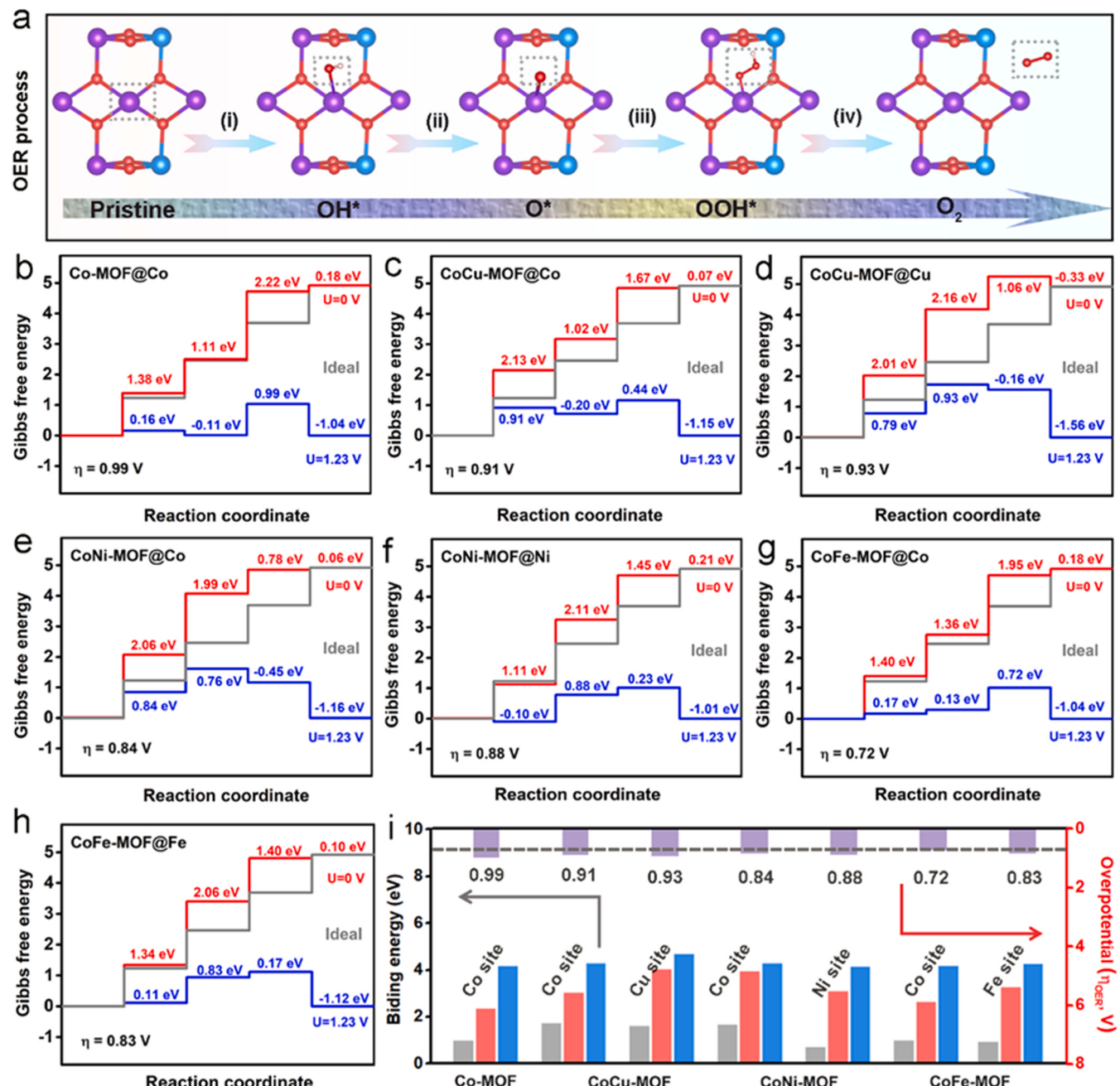


Fig. 5. a) Typical OER reaction pathway of CoFe-MOF, including the adsorption, dissociation, and desorption of reaction intermediates. The free energy profiles along the typical OER pathway on b) Co site in Co-MOF, c) Co site in CoCu-MOF, d) Cu site in CoCu-MOF, e) Co site in CoNi-MOF, f) Ni site in CoNi-MOF, g) Co site in CoFe-MOF, h) Fe site in CoFe-MOF. The reaction free energies at 0 V are marked in the red line, and 1.23 V is marked in the blue line. Ideal steps of 1.23 eV are also shown with gray lines for comparison. i) Summary of binding energy between the active center and reaction intermediates (from the left to right show the E_{OH^*} , E_{O^*} , and E_{OOH^*}), as well as the calculated overpotential for the active sites in Co-MOF and CoM-MOFs.

calculated. These include the E_d for central Co sites, E_d for substituted M, the average E_d for both central Co sites and substituted M, the average E_d for all the Co sites, as well as the average E_d for all transition metal atoms within MOF structure. The corresponding data are summarized in Fig. 6e, from which different E_d energy levels can be observed for the five E_d types. This result indicates that the electronic structure can be customized by altering the local microenvironment within the MOF structure. Furthermore, the E_d energy level plots as a function of calculated overpotential are constructed to gain insights into the correlation between the electronic structure and OER activity. The calculated OER overpotential exhibits a volcano-shaped correlation specifically with the average E_d for both central Co sites and substituted

M, which is well aligned with the reported Sabatier principle, i.e., the moderate adsorption and desorption energies of reaction intermediates are crucial for catalytic activity (Fig. S28). It is evident that no similar correlation can be captured for the other four E_d types (Fig. S29). These findings suggest only the asymmetric Co-O-M electronic structure is of paramount significance in fine-tuning the OER activity. Notably, the interaction between the 3d states of Co and M can be demonstrated by a significant overlap shown in Fig. 6f. Specifically, the CoFe-MOF with Co-O-Fe unit is situated near the summit of the volcano-shaped curves, exhibiting the optimal E_d energy level at -1.32 eV (Fig. 6g). Such optimized energy levels enable appropriate adsorption/desorption abilities for reaction intermediates, thereby resulting in superior OER

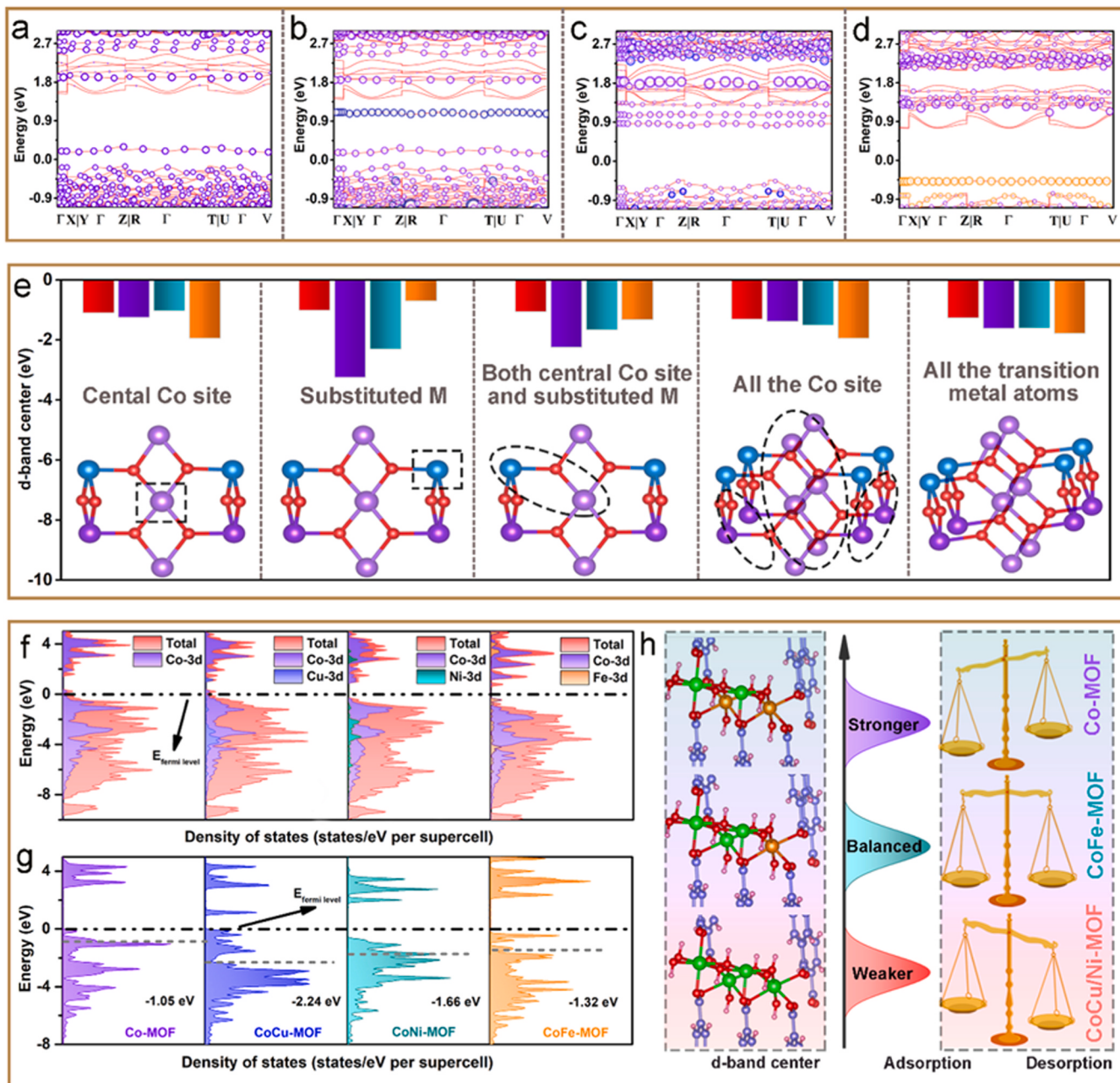


Fig. 6. The calculated band structure of Co-MOF, b) CoCu-MOF, c) CoNi-MOF, d) CoFe-MOF. e) The summary of calculated E_d values based on various coordination microenvironments within the MOF structure. f) Projected density of states and g) average E_d for both active Co sites and substituted M for Co-MOF, CoCu-MOF, CoNi-MOF and CoFe-MOF. Dashed-dotted lines and the numbers show the position of E_d energy level. h) The correlation of the average E_d for both active Co sites and substituted M against the adsorption/desorption ability of oxygen-related species (OH^+ , O^{2-} , and OOH^\bullet).

activity (Fig. 6h). For Co-MOF with Co-O-Co unit, the E_d energy level is determined to be -1.05 eV , which is higher than that of in CoFe-MOF. The elevated E_d energy levels result in a decreased electron filling of antibonding states, strengthening the binding between the Co-MOF surface and oxygen-related intermediates. This excessive binding, in turn, impedes the desorption of O_2 . The CoCu-MOF and CoNi-MOF show the E_d energy level of -2.24 and -1.66 eV , respectively, which is lower than that of CoFe-MOF. The decreased E_d energy levels would lead to weak bonding to the reaction intermediates, hindering their adsorption on the CoCu-MOF and CoNi-MOF. Therefore, it is crucial to maintain an appropriate E_d energy level to ensure a balanced adsorption/desorption ability of intermediates (OH^+ , O^{2-} , and OOH^\bullet) for the development of efficient catalysts in catalyzing OER [6].

4. Conclusion

In summary, an energy band engineering strategy is proposed to facilitate the elucidation of the relationship between the asymmetric electronic structure and the catalytic OER activity for CoM-MOFs ($M=\text{Cu, Ni, and Fe}$). The asymmetric Co-O-M electronic structure can be customized by altering the MOF local microenvironment through local symmetry-breaking. A volcano-shaped relationship is well established to depict the OER activity against the average E_d for both central Co sites and substituted M, which highlights the key role of asymmetric Co-O-M structure in fine-tuning the OER activity. The CoFe-MOF with asymmetric Co-O-Fe unit, positioned near the summit of the volcano-shaped curves, demonstrates the appropriate adsorption/desorption

capabilities of oxygen-related intermediates, thereby enhancing the OER activity. This work offers exciting new perspectives on energy band engineering in facilitating the comprehension between asymmetric electronic structure and adsorption behavior, providing valuable guidance for the rational design of high-efficiency MOF-based catalysts.

CRediT authorship contribution statement

Jian Zhou: Writing – original draft, Methodology, Investigation, Formal analysis, Data curation, Conceptualization. **Zhichu Ren:** Writing – original draft, Data curation, Conceptualization. **Fei Qiao:** Conceptualization, Formal analysis, Writing – original draft. **Huiyu Gai:** Conceptualization, Software. **Shuai Qiu:** Conceptualization, Validation. **Canhui Zhang:** Conceptualization. **Xingkun Wang:** Conceptualization, Formal analysis. **Zongkun Chen:** Conceptualization, Investigation. **Heqing Jiang:** Conceptualization, Formal analysis, Funding acquisition, Supervision. **Minghua Huang:** Conceptualization, Funding acquisition, Investigation, Methodology, Validation, Writing – original draft, Writing – review & editing.

Declaration of Competing Interest

The authors declare that they have no known competing financial interests or personal relationships that could have appeared to influence the work reported in this paper.

Data availability

Data will be made available on request.

Acknowledgements

This work is financially supported by the National Natural Science Foundation of China (52261145700, 22279124), the Natural Science Foundation of Shandong Province (ZR2022ZD30), Qingdao New Energy Shandong Laboratory Open Project (QNESL OP202307) and the Fundamental Research Funds for the Central Universities (202262010).

Appendix A. Supporting information

Supplementary data associated with this article can be found in the online version at [doi:10.1016/j.apcatb.2024.124089](https://doi.org/10.1016/j.apcatb.2024.124089).

References

- [1] C.F. Li, J.W. Zhao, L.J. Xie, J.Q. Wu, Q. Ren, Y. Wang, G.R. Li, Surface-adsorbed carboxylate ligands on layered double hydroxides/metal-organic frameworks promote the electrocatalytic oxygen evolution reaction, *Angew. Chem. Int. Ed.* 60 (2021) 18129–18137.
- [2] X. Hu, Y. Min, L.-L. Ma, J.-Y. Lu, H.-C. Li, W.-J. Liu, J.-J. Chen, H.-Q. Yu, Iron-nitrogen doped carbon with exclusive presence of FeNx active sites as an efficient ORR electrocatalyst for Zn-air battery, *Appl. Catal. B Environ.* 268 (2020) 118405.
- [3] Z.H. Liu, S.B. Shi, Y.C. Ji, K. Wang, T.W. Tan, J. Nielsen, Opportunities of CO₂-based biorefineries for production of fuels and chemicals, *Green Carbon* 1 (2023) 75–84.
- [4] Y. Song, M. Sun, S. Zhang, X. Zhang, P. Yi, J. Liu, B. Huang, M. Huang, L. Zhang, Electronic modulation of metal-organic frameworks by interfacial bridging for efficient pH-universal hydrogen evolution, *Adv. Funct. Mater.* 33 (2023) 2210322.
- [5] S. Zhang, C. Tan, R. Yan, X. Zou, F.L. Hu, Y. Mi, C. Yan, S. Zhao, Constructing built-in electric field in heterogeneous nanowire arrays for efficient overall water electrolysis, *Angew. Chem. Int. Ed.* 62 (2023) e202302795.
- [6] S. Sun, X. Zhou, B. Cong, W. Hong, G. Chen, Tailoring the d-band centers endows (Ni_xFe_{1-x})₂P nanosheets with efficient oxygen evolution catalysis, *ACS Catal.* 10 (2020) 9086–9097.
- [7] H. Xu, H.Y. Shang, C. Wang, Y.K. Du, Surface and interface engineering of noble-metal-free electrocatalysts for efficient overall water splitting, *Coord. Chem. Rev.* 418 (2020) 213374.
- [8] M.C. Luo, S.J. Guo, Strain-controlled electrocatalysis on multimetallic nanomaterials, *Nat. Rev. Mater.* 2 (2017) 17059.
- [9] X.B. Hou, Z.K. Han, X.J. Xu, D. Sarker, J. Zhou, M.A. Wu, Z.C. Liu, M.H. Huang, H. Q. Jiang, Controllable amorphization engineering on bimetallic metal-organic frameworks for ultrafast oxygen evolution reaction, *Chem. Eng. J.* 418 (2021) 129330.
- [10] Y. Wang, Y.Z. Zhang, Y.Q. Gao, G. Sheng, J.E. ten Elshof, Defect engineering of MnO₂ nanosheets by substitutional doping for printable solid-state micro-supercapacitors, *Nano Energy* 68 (2020) 104306.
- [11] M. Liu, L. Kong, X. Wang, J. He, J. Zhang, J. Zhu, X.-H. Bu, Deciphering of advantageous electrocatalytic water oxidation behavior of metal-organic framework in alkaline media, *Nano Res.* 14 (2021) 4680–4688.
- [12] Y. Wang, X. Lei, B. Zhang, B. Bai, P. Das, T. Azam, J. Xiao, Z.S. Wu, Breaking the Ru-O-Ru symmetry of a RuO₂ catalyst for sustainable acidic water oxidation, *Angew. Chem. Int. Ed.* 63 (2024) e202316903.
- [13] D. Li, B. Wang, X. Long, W. Xu, Y. Xia, D. Yang, X. Yao, Controlled asymmetric charge distribution of active centers in conjugated polymers for oxygen reduction, *Angew. Chem. Int. Ed.* 60 (2021) 26483–26488.
- [14] X. Wang, X. Zhou, C. Li, H. Yao, C. Zhang, J. Zhou, R. Xu, L. Chu, H. Wang, M. Gu, H. Jiang, M. Huang, Asymmetric Co-N₃P₁ trifunctional catalyst with tailored electronic structures enabling boosted activities and corrosion resistance in an uninterrupted seawater splitting system, *Adv. Mater.* 34 (2022) e2204021.
- [15] J.C. Dong, Y.Y. Liu, J.J. Pei, H.J. Li, S.F. Ji, L. Shi, Y.N. Zhang, C. Li, C. Tang, J. W. Liao, S.Q. Xu, B.H. Zhang, Q. Li, S.L. Zhao, Continuous electroproduction of formate via CO₂ reduction on local symmetry-broken single-atom catalysts, *Nat. Commun.* 14 (2023) 6849.
- [16] S.L. Zhao, C.H. Tan, C.T. He, P.F. An, F. Xie, S. Jiang, Y.F. Zhu, K.H. Wu, B. W. Zhang, H.J. Li, J. Zhang, Y. Chen, S.Q. Liu, J.C. Dong, Z.Y. Tang, Structural transformation of highly active metal-organic framework electrocatalysts during the oxygen evolution reaction, *Nat. Energy* 5 (2020) 881–890.
- [17] S.L. Zhao, Y. Wang, J.C. Dong, C.T. He, H.J. Yin, P.F. An, K. Zhao, X.F. Zhang, C. Gao, L.J. Zhang, J.W. Lv, J.X. Wang, J.Q. Zhang, A.M. Khattak, N.A. Khan, Z. X. Wei, J. Zhang, S.Q. Liu, H.J. Zhao, Z.Y. Tang, Ultrathin metal-organic framework nanosheets for electrocatalytic oxygen evolution, *Nat. Energy* 1 (2016) 16184.
- [18] X.X. Wang, D.Y. Du, H.Y. Xu, Y. Yan, X.J. Wen, L.F. Ren, C.Z. Shu, NiMn-based metal-organic framework with optimized e_g orbital occupancy as efficient bifunctional electrocatalyst for lithium-oxygen batteries, *Chem. Eng. J.* 452 (2023) 139524.
- [19] J. Zhou, F. Qiao, Z.C. Ren, X.B. Hou, Z.K. Chen, S.X. Dai, G. Su, Z.W. Cao, H. Q. Jiang, M.H. Huang, Amorphization engineering of bimetallic metal-organic frameworks identify volcano-type trend toward oxygen evolution reaction, *Adv. Funct. Mater.* 1 (2023) 2304380.
- [20] C. Fan, X. Wang, X.R. Wu, Y.S. Chen, Z.X. Wang, M. Li, D.M. Sun, Y.W. Tang, G. T. Fu, Neodymium-evoked valence electronic modulation to balance reversible oxygen electrocatalysis, *Adv. Energy Mater.* 13 (2023) 2203244.
- [21] M. Li, X. Wang, K. Liu, H.M. Sun, D.M. Sun, K. Huang, Y.W. Tang, W. Xing, H. Li, G. T. Fu, Reinforcing Co-O covalency via Ce(4f)-O(2p)-Co(3d) gradient orbital coupling for high-efficiency oxygen evolution, *Adv. Mater.* 35 (2023) e2302462.
- [22] H. Yao, X. Wang, K. Li, C. Li, C. Zhang, J. Zhou, Z. Cao, H. Wang, M. Gu, M. Huang, H. Jiang, Strong electronic coupling between ruthenium single atoms and ultrafine nanoclusters enables economical and effective hydrogen production, *Appl. Catal. B Environ.* 312 (2022) 121378.
- [23] J. Han, H. Bao, J.-Q. Wang, L. Zheng, S. Sun, Z.L. Wang, C. Sun, 3D N-doped ordered mesoporous carbon supported single-atom Fe-N-C catalysts with superior performance for oxygen reduction reaction and zinc-air battery, *Appl. Catal. B Environ.* 280 (2021) 119411.
- [24] W.Q.Q. Zheng, R. Zhu, H.J.J. Wu, T. Ma, H.J.J. Zhou, M. Zhou, C. He, X.K.K. Liu, S. Li, C. Cheng, Tailoring bond microenvironments and reaction pathways of single-atom catalysts for efficient water electrolysis, *Angew. Chem. Int. Ed.* 61 (2022) e202208667.
- [25] J.L. Chen, G.F. Qian, B.X. Chu, Z.X. Jiang, K.X. Tan, L. Luo, B. Li, S.B. Yin, Tuning d-band center of Pt by PtCo-PtSn heterostructure for enhanced oxygen reduction reaction performance, *Small* 18 (2022) 2106773.
- [26] J.J. Wu, Z.Z. Wang, X. Jin, S. Zhang, T. Li, Y.H. Zhang, H. Xing, Y. Yu, H.G. Zhang, X.F. Gao, H. Wei, Hammett relationship in oxidase-mimicking metal-organic frameworks revealed through a protein-engineering-inspired strategy, *Adv. Mater.* 33 (2021) 2005024.
- [27] Z.Y. Chen, Y. Song, J.Y. Cai, X.S. Zheng, D.D. Han, Y.S. Wu, Y.P. Zang, S.W. Niu, Y. Liu, J.F. Zhu, X.J. Liu, G.M. Wang, Tailoring the d-band centers enables Co4N nanosheets to be highly active for hydrogen evolution catalysis, *Angew. Chem. Int. Ed.* 57 (2018) 5076–5080.
- [28] T. Rodenas, I. Luz, G. Prieto, B. Seoane, H. Miro, A. Corma, F. Kapteijn, I.X.F. X. Llabrés, J. Gascon, Metal-organic framework nanosheets in polymer composite materials for gas separation, *Nat. Mater.* 14 (2015) 48–55.
- [29] M. Li, H.C. Sun, J.M. Yang, M. Humayun, L.F. Li, X.F. Xu, X.Y. Xue, A. Habibi-Yangjeh, K. Temst, C.D. Wang, *Chem. Eng. J.* 430 (2022) 132733.
- [30] X. Hou, Z. Han, X. Xu, D. Sarker, J. Zhou, M. Wu, Z. Liu, M. Huang, H. Jiang, Mono-coordinated metallocene ligands endow metal-organic frameworks with highly efficient oxygen evolution and urea electrolysis, *Chem. Eng. J.* 418 (2021) 129330.
- [31] J.T. Li, W.Z. Huang, M.M. Wang, S.B. Xi, J.S. Meng, K.N. Zhao, J. Jin, W.W. Xu, Z. Y. Wang, X. Liu, Q. Chen, L.H. Xu, X.B. Liao, Y.L. Jiang, K.A. Owusu, B.L. Jiang, C. X. Chen, D.N.A. Fan, L. Zhou, L.Q. Mai, Low-crystalline bimetallic metal-organic framework electrocatalysts with rich active sites for oxygen evolution, *ACS Energy Lett.* 4 (2019) 285–292.
- [32] W.J. Li, S. Xue, S. Watzle, S.J. Hou, J. Fichtner, A.L. Semrau, L.J. Zhou, A. Welle, A.S. Bandarenka, R.A. Fischer, Advanced bifunctional oxygen reduction and evolution electrocatalyst derived from surface-mounted metal-organic frameworks, *Angew. Chem. Int. Ed.* 59 (2020) 5837–5843.

- [33] F. Sun, G. Wang, Y. Ding, C. Wang, B. Yuan, Y. Lin, NiFe-based metal-organic framework nanosheets directly supported on nickel foam acting as robust electrodes for electrochemical oxygen evolution reaction, *Adv. Energy Mater.* 8 (2018) 1800584.
- [34] H. Gai, S. Xue, X. Wang, J. Zhou, H. Jiang, M. Huang, Sandwich-like hierarchical porous dual-carbon catalyst with more accessible sites for boosting oxygen reduction reaction, *Mater. Today Energy* 21 (2021) 100809.
- [35] Y. Shao, J. Sui, G. Yin, Y. Gao, Nitrogen-doped carbon nanostructures and their composites as catalytic materials for proton exchange membrane fuel cell, *Appl. Catal. B Environ.* 79 (2008) 89–99.
- [36] H. Li, J. Wang, R. Qi, Y. Hu, J. Zhang, H. Zhao, J. Zhang, Y. Zhao, Enhanced Fe 3d delocalization and moderate spin polarization in Fe-Ni atomic pairs for bifunctional ORR and OER electrocatalysis, *Appl. Catal. B Environ.* 285 (2021) 119778.
- [37] J.S. Meng, Q. He, L.H. Xu, X.C. Zhang, F. Liu, X.P. Wang, Q. Li, X.M. Xu, G. B. Zhang, C.J. Niu, Z.T. Xiao, Z. Liu, Z.Z. Zhu, Y. Zhao, L.Q. Mai, Identification of phase control of carbon-confined Nb₂O₅ nanoparticles toward high-performance lithium storage, *Adv. Energy Mater.* 9 (2019) 1802695.
- [38] D. Senthil Raja, X.-F. Chuah, S.-Y. Lu, In Situ grown bimetallic MOF-based composite as highly efficient bifunctional electrocatalyst for overall water splitting with ultrastability at high current densities, *Adv. Energy Mater.* 8 (2018) 1801065.
- [39] J. Zhou, Z. Han, X. Wang, H. Gai, Z. Chen, T. Guo, X. Hou, L. Xu, X. Hu, M. Huang, S.V. Levchenko, H. Jiang, Discovery of quantitative electronic structure-OER activity relationship in metal-organic framework electrocatalysts using an integrated theoretical-experimental approach, *Adv. Funct. Mater.* 31 (2021) 2102066.
- [40] K.H. Wu, Y. Liu, X. Tan, Y. Liu, Y. Lin, X. Huang, Y. Ding, B.-J. Su, B. Zhang, J.-M. Chen, W. Yan, S.C. Smith, I.R. Gentle, S. Zhao, Regulating electron transfer over asymmetric low-spin Co (II) for highly selective electrocatalysis, *Chem. Catal.* 2 (2022) 372–385.
- [41] Y. Liu, Y. Wang, S. Zhao, Z. Tang, Metal-organic framework-based nanomaterials for electrocatalytic oxygen evolution, *Small Methods* 6 (2022) e2200773.
- [42] Y. Yang, Y. Yang, Y. Liu, S. Zhao, Z. Tang, Metal-organic frameworks for electrocatalysis: beyond their derivatives, *Small Sci.* 1 (2021) 2100015.
- [43] X. Wang, X.J. Gao, L. Qin, C. Wang, L. Song, Y.N. Zhou, G. Zhu, W. Cao, S. Lin, L. Zhou, K. Wang, H. Zhang, Z. Jin, P. Wang, X. Gao, H. Wei, eg occupancy as an effective descriptor for the catalytic activity of perovskite oxide-based peroxidase mimics, *Nat. Commun.* 10 (2019) 704.
- [44] B. Fei, Z.L. Chen, J.X. Liu, H.B. Xu, X.X. Yan, H.L. Qing, M. Chen, R.B. Wu, Ultrathinning nickel sulfide with modulated electron density for efficient water splitting, *Adv. Energy Mater.* 10 (2020) 2001963.
- [45] C.X. Zhang, Q.L. Qi, Y.J. Mei, J. Hu, M.Z. Sun, Y.J. Zhang, B.L. Huang, L.B. Zhang, S.H. Yang, Rationally reconstructed metal-organic frameworks as robust oxygen evolution electrocatalysts, *Adv. Mater.* 35 (2023) 2208904.
- [46] Y. Xu, S. Wei, L. Gan, L. Zhang, F. Wang, Q. Wu, X. Cui, W. Zheng, Conversion of 2D MXene to multi-low-dimensional GeRMXene superlattice heterostructure, *Adv. Funct. Mater.* 32 (2022) 2112623.
- [47] R. Ahmad, N. Iqbal, T. Noor, G. Ali, M. Ali, N. Shahzad, M.A. Raza, Zeolitic imidazolate frameworks derived Co-Zn-nanoporous carbon-sulfide material for supercapacitors, *Electrochim. Acta* 404 (2022) 139739.
- [48] N. Zaman, N. Iqbal, T. Noor, An efficient and stable electrocatalyst derived from Ni-Mo-Co MOF for methanol oxidation reaction, *ChemCatChem* 15 (2023) e202300502.
- [49] W. Ahmad, T. Noor, M. Zeeshan, Effect of synthesis route on catalytic properties and performance of Co₃O₄/TiO₂ for carbon monoxide and hydrocarbon oxidation under real engine operating conditions, *Catal. Commun.* 89 (2017) 19–24.
- [50] W. Zheng, L.Y.S. Lee, Metal-organic frameworks for electrocatalysis: catalyst or precatalyst? *ACS Energy Lett.* 6 (2021) 2838–2843.
- [51] L. Zhong, J. Ding, X. Wang, L. Chai, T.T. Li, K. Su, Y. Hu, J. Qian, S. Huang, Structural and morphological conversion between two Co-based MOFs for enhanced water oxidation, *Inorg. Chem.* 59 (2020) 2701–2710.
- [52] S. Ashraf, R. Mehek, N. Iqbal, T. Noor, G. Ali, A. Wahab, A.A. Qayyum, A. Ahmad, ZIF 67 derived Co-Si composites with N-doped nanoporous carbon as anode material for Li-ion batteries, *Mater. Chem. Phys.* 270 (2021) 124824.
- [53] M. Habib Ur Rehman, T. Noor, N. Iqbal, Effect of zirconia on hydrothermally synthesized Co₃O₄/TiO₂ catalyst for NOx reduction from engine emissions, *Catalysts* 10 (2020) 209.
- [54] N. Zaman, N. Iqbal, T. Noor, Comparative study of Mn-ZIF-67 derived carbon (Mn-Co/C) and its rGO-based composites for the methanol oxidation, *J. Environ. Chem. Eng.* 10 (2022) 108351.
- [55] A. Wahab, N. Iqbal, T. Noor, S. Ashraf, M.A. Raza, A. Ahmad, U.A. Khan, Thermally reduced mesoporous manganese MOF@reduced graphene oxide nanocomposite as bifunctional electrocatalyst for oxygen reduction and evolution, *RSC Adv.* 10 (2020) 27728–27742.
- [56] C. Han, L. Zhong, Q. Sun, D. Chen, T.-T. Li, Y. Hu, J. Qian, S. Huang, Electrochemical evolution of cobalt-carboxylate framework for efficient water oxidation, *J. Power Sources* 499 (2021) 229947.
- [57] S. Xu, H. Ni, X. Zhang, C. Han, J. Qian, Abundant surface defects in cobalt hydroxides/oxyhydroxides induced by zinc species facilitate water oxidation, *Inorg. Chem.* 62 (2023) 14757–14763.
- [58] J. Yu, C. Su, L. Shang, T. Zhang, Single-atom-based oxygen reduction reaction catalysts for proton exchange membrane fuel cells: progress and perspective, *ACS Nano* 17 (2023) 19514–19525.
- [59] H. Liu, M. Jin, D. Zhan, J. Wang, X. Cai, Y. Qiu, L. Lai, Stacking faults triggered strain engineering of ZIF-67 derived Ni-Co bimetal phosphide for enhanced overall water splitting, *Appl. Catal. B Environ.* 272 (2020) 118951.
- [60] Y. Dou, C.-T. He, L. Zhang, M. Al-Mamun, H. Guo, W. Zhang, Q. Xia, J. Xu, L. Jiang, Y. Wang, P. Liu, X.-M. Chen, H. Yin, H. Zhao, How cobalt and iron doping determine the oxygen evolution electrocatalytic activity of NiOOH, *Cell Rep. Phys. Sci.* 1 (2020) 100077.
- [61] M. Li, L. Feng, NiSe₂-CoSe₂ with a hybrid nanorods and nanoparticles structure for efficient oxygen evolution reaction, *Chin. J. Struct. Chem.* 41 (2022) 2201019–2201024.
- [62] X. Hou, T. Jiang, X. Xu, X. Wang, J. Zhou, H. Xie, Zhicheng Liu, L. Chu, M. Huang, Coupling of NiFe-based metal-organic framework nanosheet arrays with embedded Fe-Ni₃S₂ clusters as efficient bifunctional electrocatalysts for overall water splitting, *Chin. J. Struct. Chem.* 41 (2022) 2207074–2207080.
- [63] M. Xiao, C. Wu, J. Zhu, C. Zhang, Y. Li, J. Lyu, W. Zeng, H. Li, L. Chen, S. Mu, In situ generated layered NiFe-LDH/MOF heterostructure nanosheet arrays with abundant defects for efficient alkaline and seawater oxidation, *Nano Res.* 16 (2023) 8945–8952.